Spin Seebeck effect and thermal properties of zigzag graphene nanoribbons with edge magnetism

Jing Li, Yann-Michel Niquet, Christophe Delerue

Spin Seebeck effect and thermal properties of zigzag graphene nanoribbons with edge magnetism

Jing Li [1,*] Yann-Michel Niquet [2] and Christophe Delerue [3]
[1]*Université Grenoble Alpes, CEA, Leti, F-38000 Grenoble, France*
[2]*Université Grenoble Alpes, CEA, IRIG-MEM-L_Sim, F-38000 Grenoble, France*
[3]*Université Lille, Centre National de la Recherche Scientifique, Université Polytechnique Hauts-de-France, Centrale Lille, Junia, UMR 8520-IEMN, F-59000 Lille, France*

(Received 5 May 2023; accepted 6 June 2023; published 14 June 2023)

Zigzag graphene nanoribbons (GNRs), demonstrating edge magnetism, are fascinating materials for electronic and spintronic applications. In this paper, we investigate with explicit consideration of electron-phonon scattering the Seebeck effect and thermal conductivity at various carrier densities in zigzag GNRs, which undergo antiferromagnetic, ferromagnetic, and paramagnetic transitions. Seebeck coefficients are spin dependent in ferromagnetic zigzag GNRs and can have opposite signs for the majority and the minority spin carriers, which enables the separation of spin carriers spatially under a thermal gradient. The electronic thermal conductivity is small compared to the lattice thermal conductivity, except for GNRs in the ferromagnetic state. A 100% increase in thermal conductivity is expected at antiferromagnetic to ferromagnetic transition. These results demonstrate that zigzag GNRs are also materials of high interest for spin caloritronics.

DOI: 10.1103/PhysRevB.107.245417

I. INTRODUCTION

Graphene nanoribbons (GNRs), ribbons of graphene with a width in the nanometer range, are attractive materials for many applications, such as electronics and spintronics [1–3]. Made of carbon with sp^2 hybridization, GNRs can be obtained as graphene cuttings or unzipped carbon nanotubes [4,5]. GNRs can also be produced using bottom-up approaches, which lead to outstanding edge control [6–8]. Indeed, the edge of a GNR significantly influences its physical properties, especially its electronic structure, which can be metallic or semiconducting [9–11]. The edge geometry is defined by the chiral angle of the ribbon, which can take any value between 0° and 30°. Here we consider zigzag GNRs (chiral angle of 0°), for which extremely rich electronic and magnetic phases have been predicted.

Theoretical studies have shown that zigzag GNRs have strongly localized edge states [10], which bring magnetism as spins tend to align along each edge [9,12]. But the coupling between opposite edges depends on GNR width and carrier density [13,14]. Half filling leads to an antiferromagnetic (AF) state, i.e., opposite spins on opposite edges. By increasing carrier density, a ferromagnetic (F) phase can be reached with the same spin on both edges when edge states remain partially filled, and a paramagnetic (P) phase is finally obtained when these edge states are fully occupied. Some experiments indirectly confirmed these predictions. The abrupt vanishing of the electronic gap in zigzag GNRs with increasing ribbon width was ascribed to the AF to F transition [15]. A single conducting channel, characterized by half of the quantum conductance in the ballistic regime and by a mean free path up to micrometers at room temperature [16,17], points towards the GNR in the F state, as was later explained by transport with spin-dependent electron-phonon scattering [14]. Recently, the edge magnetism in zigzag GNRs was probed directly by a nitrogen atom which substitutes a carbon atom at the GNR edge [18]. Based on these facts, zigzag GNRs with edge magnetism are fascinating not only for electronic applications because of their extraordinary electron transport properties, such as two orders of magnitude enhancement in electron conduction at the AF to F transition, but also for spintronic applications, due to their spin-dependent transport properties such as a 100% spin-filtering factor [14].

These properties, together with the weak spin-orbit coupling, make zigzag GNRs promising materials for spin caloritronics, which describes the conversion between heat and spin current [19]. The spin Seebeck effect or its reverse effect, namely, the spin Peltier effect, has been observed in metals, semiconductors, and insulators [20–25]. Experimental work on spin caloritronics of zigzag GNRs is missing, and theoretical studies were focused on short ribbon length in the ballistic regime [26–30], which is hard to realize experimentally. In this paper, we present a study of the spin Seebeck effect and thermal properties of zigzag GNRs taking into account all electron-phonon scattering processes at room temperature. The mean free paths are also reported, which will help design devices operating in ballistic or diffusive regimes depending on their length.

II. THEORY

A. Two current model

The two current model describes independent majority and minority spin channels [31,32]. Defining majority carriers as spin up, the charge current I_α, where α represents spin ($\uparrow$, $\downarrow$),

*jing.li@cea.fr

and heat current $\dot{Q}_\alpha$ are described by the following equation:

$$\begin{bmatrix} I_\uparrow \\ \dot{Q}_\uparrow \\ I_\downarrow \\ \dot{Q}_\downarrow \end{bmatrix} = \begin{bmatrix} L_\uparrow^{1,1} & L_\uparrow^{1,2} & 0 & 0 \\ L_\uparrow^{2,1} & L_\uparrow^{2,2} & 0 & 0 \\ 0 & 0 & L_\downarrow^{1,1} & L_\downarrow^{1,2} \\ 0 & 0 & L_\downarrow^{2,1} & L_\downarrow^{2,2} \end{bmatrix} \begin{bmatrix} \xi_\uparrow^e \\ -\nabla T_\uparrow \\ \xi_\downarrow^e \\ -\nabla T_\downarrow \end{bmatrix}, \quad (1)$$

where ξ_α^e is an effective electric field and $-\nabla T_\alpha$ is a temperature gradient. The effective electric field comprises the electric field ξ and the gradient of spin-dependent chemical potential [33], $\nabla\mu_\alpha$, i.e.,

$$\xi_\alpha^e = \xi_\alpha + \frac{\nabla\mu_\alpha}{e}, \quad (2)$$

where e is the unit charge. The absence of a spin-flip mechanism [zero nondiagonal blocks in the matrix of Eq. (1)] is justified by the weak spin-orbit coupling that leads to long-distance spin transport in graphene [34,35].

The matrix elements $L_\alpha^{1,1}$ and $L_\alpha^{2,1}$ are determined by [36]

$$L_\alpha^{1,1} = -e^2 \sum_b \int g_{b,\alpha}^{(\xi^e)}(k) v_{b,\alpha}(k) dk, \quad (3)$$

$$L_\alpha^{2,1} = e \sum_b \int (E_{k,b,\alpha} - \mu_\alpha) g_{b,\alpha}^{(\xi^e)}(k) v_{b,\alpha}(k) dk, \quad (4)$$

where $v_{b,\alpha}(k)$ is the group velocity of the electronic state at wave vector k in band b, and $g_{b,\alpha}^{(\xi^e)}(k)$ is the first-order response of the carrier distribution function to the effective electric field, namely,

$$f_{b,\alpha}^{(\xi^e)}(k) = f^0(E_{k,b,\alpha}) + e\xi_\alpha^e g_{b,\alpha}^{(\xi^e)}(k), \quad (5)$$

with f^0 the Fermi-Dirac distribution function, and $E_{k,b,\alpha}$ the energy of the electronic state $|k, b, \alpha\rangle$. Similarly, $L_\alpha^{1,2}$ and $L_\alpha^{2,2}$ are expressed as

$$L_\alpha^{1,2} = -e \sum_b \int g_{b,\alpha}^{(-\nabla T)}(k) v_{b,\alpha}(k) dk, \quad (6)$$

$$L_\alpha^{2,2} = \sum_b \int (E_{k,b,\alpha} - \mu_\alpha) g_{b,\alpha}^{(-\nabla T)}(k) v_{b,\alpha}(k) dk, \quad (7)$$

where $g_{b,\alpha}^{(-\nabla T)}(k)$ is the first-order response to a temperature gradient:

$$f_{b,\alpha}^{(-\nabla T)}(k) = f^0(E_{k,b,\alpha}) - \nabla T_\alpha g_{b,\alpha}^{(-\nabla T)}(k). \quad (8)$$

These four matrix elements characterize the transport properties. The spin-dependent electric conductivity is simply

$$\sigma_\alpha = L_\alpha^{1,1}. \quad (9)$$

The spin Seebeck coefficient is the ratio between the generated effective electric field and the temperature gradient, evaluated in an open circuit ($I_\alpha = 0$):

$$S_\alpha = -\frac{\xi_\alpha^e}{-\nabla T_\alpha} = \frac{L_\alpha^{1,2}}{L_\alpha^{1,1}}. \quad (10)$$

The spin-dependent thermal conductivity by charge carriers is the ratio between the heat current and the temperature gradient, also evaluated at an open circuit:

$$K_\alpha = \frac{\dot{Q}_\alpha}{-\nabla T_\alpha} = L_\alpha^{2,2} - L_\alpha^{2,1}\left(L_\alpha^{1,1}\right)^{-1} L_\alpha^{1,2}, \quad (11)$$

where the term $-L_\alpha^{2,1}(L_\alpha^{1,1})^{-1}L_\alpha^{1,2}$ accounts for the heat current driven by the effective electric field generated by the temperature gradient through the Seebeck effect.

B. Spin-charge representation

In spin-charge representation, the charge current I_c and spin current I_s are defined as

$$I_c = I_\uparrow + I_\downarrow \quad I_s = I_\uparrow - I_\downarrow. \quad (12)$$

The charge heat current $\dot{Q}_c$ and spin heat current $\dot{Q}_s$ are defined similarly:

$$\dot{Q}_c = \dot{Q}_\uparrow + \dot{Q}_\downarrow \qquad \dot{Q}_s = \dot{Q}_\uparrow - \dot{Q}_\downarrow. \quad (13)$$

The charge and spin components of the effective electric field and temperature gradient are given by the following averages and differences:

$$\xi_c^e = \frac{\xi_\uparrow^e + \xi_\downarrow^e}{2}, \quad \xi_s^e = \xi_\uparrow^e - \xi_\downarrow^e, \quad (14)$$

$$T_c = \frac{T_\uparrow + T_\downarrow}{2}, \quad T_s = T_\uparrow - T_\downarrow. \quad (15)$$

With the above definitions, Eq. (1) turns into

$$\begin{bmatrix} I_c \\ \dot{Q}_c \\ I_s \\ \dot{Q}_s \end{bmatrix} = \begin{bmatrix} L_+^{1,1} & L_+^{1,2} & L_-^{1,1} & L_-^{1,2} \\ L_+^{2,1} & L_+^{2,2} & L_-^{2,1} & L_-^{2,2} \\ L_-^{1,1} & L_-^{1,2} & L_+^{1,1} & L_+^{1,2} \\ L_-^{2,1} & L_-^{2,2} & L_+^{2,1} & L_+^{2,2} \end{bmatrix} \begin{bmatrix} \xi_c^e \\ -\nabla T_c \\ \xi_s^e/2 \\ -\nabla T_s/2 \end{bmatrix}, \quad (16)$$

where $L_\pm^{i,j} = L_\uparrow^{i,j} \pm L_\downarrow^{i,j}$ with $i, j = 1$ or 2. The off-diagonal block $L_-^{i,j}$ describes the conversion between charge and spin by a temperature gradient or an effective electric field.

C. Numerical simulations

The electronic structure of zigzag GNRs is described by a mean-field Hubbard tight-binding model [14,15]:

$$H = \sum_i E_{i,\sigma}\hat{n}_{i,\sigma} + \sum_{i,j,\sigma} t_{i,j}\hat{c}_{i,\sigma}^\dagger \hat{c}_{j,\sigma} + U\sum_i (\hat{n}_{i,\uparrow}\langle n_{i,\downarrow}\rangle + \hat{n}_{i,\downarrow}\langle n_{i,\uparrow}\rangle - \langle n_{i,\uparrow}\rangle\langle n_{i,\downarrow}\rangle), \quad (17)$$

where $\hat{c}^\dagger$ ($\hat{c}$) is the creation (annihilation) operator, $\hat{n}$ is the number operator, and i (j) is the index of an atomic site. The term E_i is the on-site energy, and $t_{i,j}$ is the hopping energy between nearest-neighbor atoms that depends on the bond length [37]. Tight-binding parameters are from Ref. [37].

The Hubbard potential U is set to the value of 3.24 eV, which reproduces the experimental band gap of zigzag GNRs [15]. The electronic structure and spin densities are solved self-consistently. Multisolutions, corresponding to different self-consistent fixed points, are obtained by using symmetric, antisymmetric, and random wave functions as initial guesses. The ground state is chosen as the solution with the minimum free energy:

$$\Omega = -U\sum_i \langle n_{i,\uparrow}\rangle\langle n_{i,\downarrow}\rangle - \frac{k_B T}{N_k}\sum_{k,b,\alpha}\ln\left[1+\exp\left(\frac{E_{k,b,\alpha}-\mu}{k_B T}\right)\right], \tag{18}$$

where k_B is the Boltzmann constant, μ is the chemical potential, and N_k is the total number of k points sampling the first Brillouin zone.

The transport properties are determined by solving the Boltzmann equation accounting for electron-phonon scattering, which is beyond the relaxation time approximation. All electron-phonon scattering processes satisfying wave-vector conservation are taken into account explicitly. The full phonon bands of zigzag GNRs are obtained from a fourth-nearest-neighbor force-constant model [37]. Scattering rates computed using Fermi's "golden rule" are injected into the Boltzmann transport equations (BTEs). The term $g_{b,\alpha}^{(\xi^e)}(k)$ is the solution of a linearized BTE under an effective electric field [38]. Similarly, the term $g_{b,\alpha}^{(-\nabla T)}(k)$ is the solution of the following linearized BTE under a temperature gradient:

$$\frac{2\pi}{l}v_b(k)\left(\frac{\partial f^0}{\partial T}\right)_{E_{k,b}} = \sum_{b'}\int g_b^{(-\nabla T)}(k)\{W_{kb,k'b'}[1-f^0(E_{k',b'})]+W_{k'b',kb}f^0(E_{k',b'})\} - g_{b'}^{(-\nabla T)}(k')\{W_{k'b',kb}[1-f^0(E_{k,b})]+W_{kb,k'b'}f^0(E_{k,b})\}dk', \tag{19}$$

where l is the length of the unit cell, and $W_{k'b',kb}$ is the scattering matrix element determined from Fermi's "golden rule" [see Eq. (3) in Ref. [38]]. With the terms $g_{b,\alpha}^{(\xi^e)}(k)$ and $g_{b,\alpha}^{(-\nabla T)}(k)$, the matrix elements $L_\sigma^{i,j}$ in Eq. 1 are determined.

III. RESULTS AND DISCUSSION

Transport properties of a zigzag GNR depend significantly on its magnetic phase, which is sensitive to the carrier density, temperature, and ribbon width [14]. In the following, we focus on a 5-nm-wide zigzag GNR at room temperature (300 K) with variable carrier density. The matrix elements of Eqs. (1) and (16), calculated numerically as described in Sec. II C, are presented in Fig. 1. It is important to note that our calculations give $L_\alpha^{1,2} = TL_\alpha^{2,1}$ as required by Onsager reciprocal relations, which translates into the relationship between Seebeck and Peltier coefficients [39].

A. Electric conductivity

With the increase of carrier concentration, the magnetic phase goes from an AF state to an F state, back to an AF state, and then to a P state [14]. The band structures and mean free paths for six selected carrier densities are shown in Fig. 2(a). The electric conductivity $L^{1,1}$ shown in Fig. 1(a) has been discussed in previous work [14]. In AF states, a finite electronic band gap exists, as shown in Figs. 2(a) and 2(e). The presence of a band gap tends to increase the effective mass and reduce the group velocity of the electrons located in the nearby band. Also, the band edge provides abundant electronic states, enhancing electron-phonon scattering. Therefore the electric conductivity is small in AF states.

In the F state, majority carriers have only one channel near the Fermi level, experiencing long-range ballistic transport, with a mean free path up to micrometers, thanks to the large group velocity [nearly linear dispersive band structure; see Figs. 2(b)–2(d)] and spin-protected transport (weak scattering). In contrast, minority carriers have three channels involved in the transport, suffering from scattering to edge bands. Two channels have a very short mean free path (approximately tens of nanometers). The other channel with a larger group velocity has a longer mean free path (approximately hundreds of nanometers). For the above reasons, the magnetic phase transition from AF to F state is accompanied by two orders of magnitude enhancement in electric conductivity [Fig. 1(a)], thanks to the long mean free path of the majority carrier in F states [14].

In P states, the Fermi level cuts bands with linear dispersion [Fig. 2(f)]. These states are far above the edge states, and below the edge of the second band, which has a large density of states. These features of the electronic structure induce a substantial reduction of the electron scattering by phonons, resulting in two conducting channels with a long mean free path up to several hundred nanometers for each spin.

B. Seebeck effects

The Seebeck effect generates an open-circuit voltage from a temperature gradient. Electrons above the Fermi level carry excess energy, flowing from the hot to the cold side. In contrast, electrons below the Fermi level flow in the opposite direction, as described by the driving force $\partial f/\partial T$ induced by the temperature gradient shown in Figs. 3(b) and 3(d), in contrast to the unidirectional electron transport induced by the effective electric field [Fig. 3(c)]. A material with balanced electron transport below and above the Fermi level would not create open-circuit voltage, hence no Seebeck effect. The Seebeck coefficient of graphene is, therefore, zero at the Dirac point, and reaches a peak value of about 90 μV/K at room temperature by varying the carrier density [40].

Figure 3(a) describes the Seebeck effect in zigzag GNRs. At low carrier density in the AF state, the Seebeck coefficient

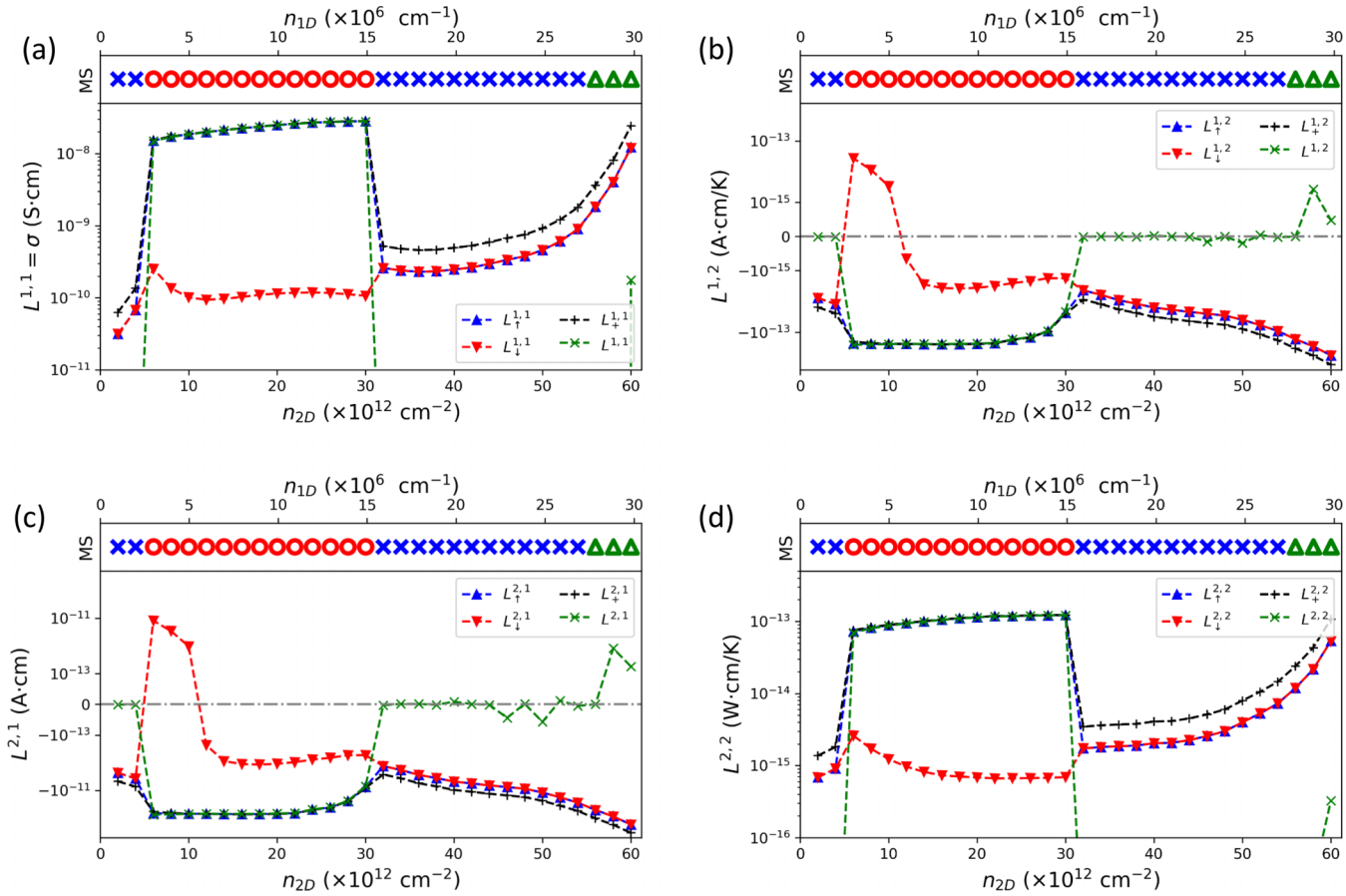

FIG. 1. Transport matrix elements defined in Eqs. (1) and (16) for a 5-nm-wide zigzag GNR at 300 K vs carrier density. Magnetic states are indicated for each density at the top of each figure by symbols (blue cross, AF; red circle, F; green triangle, P). The electrical conductivity is $L^{1,1}$ shown in (a). In (b) and (c), a symmetrical log scale is used for the y axis to represent both positive and negative values.

is large, about -250 μV/K (the negative sign denotes an n-type carrier) because the Fermi level lies in the band gap, slightly below the bottom of the conduction band [Fig. 2(a)] from which nearly all the conductivity comes. At larger carrier density in AF and P states, although a band gap exists, the Fermi level lies in the conduction band [Figs. 2(e) and 2(f)]. Both electronic states below and above the Fermi level contribute to electric conduction, leading to a smaller Seebeck coefficient.

Spin Seebeck effect treats majority and minority carriers separately. In the F state, the spin-up channel (majority carriers) with a long mean free path has almost balanced conductivity above and below the Fermi level [Fig. 2(b)], which yields a small Seebeck coefficient [Fig. 3(a)]. For the spin-down channel (minority carriers), at low carrier density, the electron conduction suffers strong scattering by phonons due to the edge states above the Fermi level. Therefore most of the electric conduction occurs below the Fermi level. For this reason, the Seebeck coefficient is large, about 100 μV/K. Remarkably, $S_\downarrow$ is positive (minority p-type carriers), opposite to $S_\uparrow$ (majority n-type carriers), which means that spin-up and spin-down electrons move in opposite directions [see inset of Fig. 3(a)] and separate spatially. By increasing carrier density, the Fermi level goes into the edge states, and the conduction below the Fermi level is suppressed by the presence of edge states too [Figs. 2(c) and 2(d)], resulting in a small Seebeck coefficient of the reversed sign.

C. Thermal conductivity

The electronic contribution to the thermal conductivity [Fig. 4(a)] has the same magnetic phase dependence as the charge transport. We therefore define spin-dependent Lorenz factors as $L_\alpha = K_\alpha/(T\sigma_\alpha)$. For metals where the Wiedemann-Franz law applies [41], $L_\uparrow$ and $L_\downarrow$ take the same universal value:

$$L_0 = \frac{\pi^2}{3}\left(\frac{k_B}{e}\right)^2. \tag{20}$$

Figure 4(b) shows that the Lorenz factor in zigzag GNRs can deviate from L_0, possibly because of Umklapp intervalley scattering involving phonons with long wave vector [42]. This is the main scattering process for majority carriers in the F state, where the Lorenz factor is only half of L_0.

The lattice thermal conductivity of zigzag GNRs is about 10^{-13} W cm/K [43,44] if we consider a thickness of 3.4 Å. This is comparable to the electronic thermal conductivity in the F state. Therefore, during the AF to F transition, the total thermal conductivity doubles.

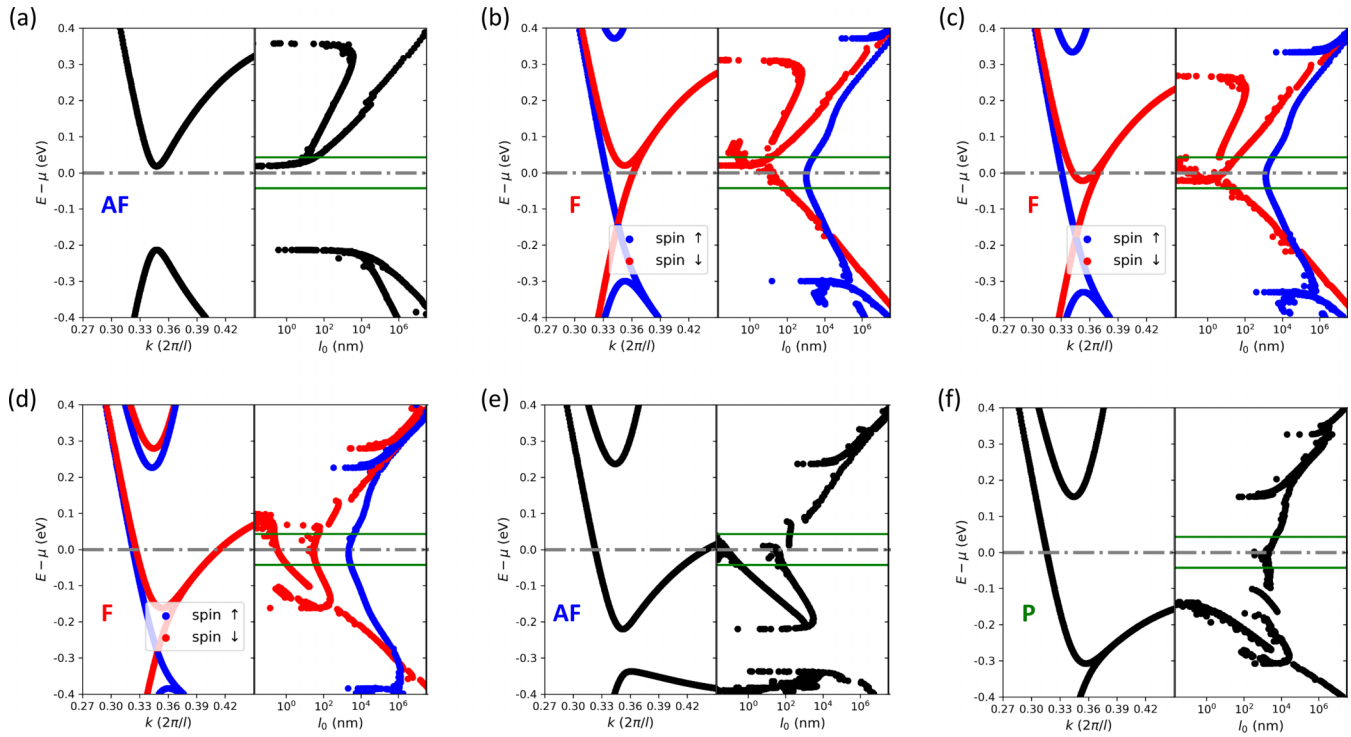

FIG. 2. Band structures (left panels) and mean free paths (right panels) of a 5-nm-wide zigzag GNR at (a) $n_{2D} = 2 \times 10^{12}$ cm^{-2} in the AF state; (b) $n_{2D} = 6 \times 10^{12}$ cm^{-2} in the F state; (c) $n_{2D} = 10 \times 10^{12}$ cm^{-2} in the F state; (d) $n_{2D} = 30 \times 10^{12}$ cm^{-2} in the F state; (e) $n_{2D} = 40 \times 10^{12}$ cm^{-2} in the AF state; and (f) $n_{2D} = 60 \times 10^{12}$ cm^{-2} in the P state. Blue (red) dots correspond to majority (minority) spin-up (spin-down) states. Black dots represent spin degenerate situations. The bands near Fermi level with $k \gtrapprox 0.35 \times 2\pi/l$ correspond to edge states, which are less dispersive [14]. The Fermi level is indicated by a horizontal dash-dotted line. The two green solid lines in mean free path plots are placed at the extrema of $\partial f/\partial T$ at $T = 300$ K, as shown in Fig. 3(b).

The generation of electricity from a thermal gradient is described by the second term of Eq. (11), i.e.,

$$L_\alpha^{2,1}(L_\alpha^{1,1})^{-1}L_\alpha^{1,2} = P_\alpha T, \tag{21}$$

which is the power factor $P_\alpha = S_\alpha^2 \sigma_\alpha$ multiplied by the temperature. This quantity is shown in Fig. 4(c), indicating more than one order of magnitude difference between the two spin channels in F states, which can be highly interesting for spin caloritronics. This term normalized by the thermal conductivity gives the figure of merit for thermoelectric applications [Fig. 4(d)]:

$$ZT = \frac{S^2 \sigma T}{K_e + K_l}. \tag{22}$$

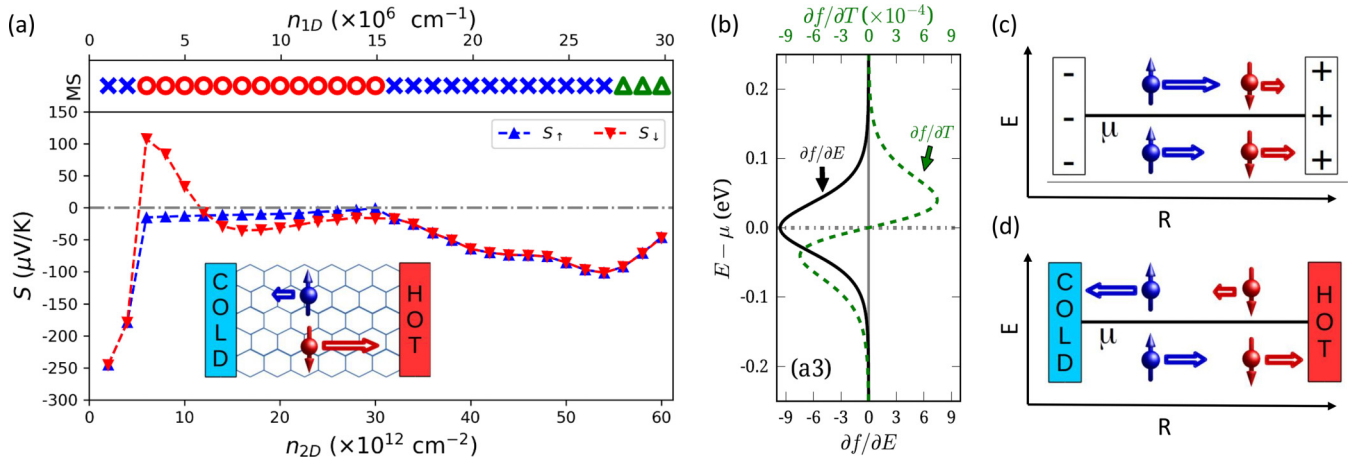

FIG. 3. (a) Spin Seebeck coefficients in a 5-nm-wide zigzag GNR at 300 K vs carrier density. Magnetic states are defined as in Fig. 1. Inset of (a): Electrons of opposite spin flow in opposite directions when spin Seebeck coefficients have opposite signs. (b) Comparison of electron flows driven by an effective electric field, $\partial f/\partial E$, and by a temperature gradient $\partial f/\partial T$ at $T = 300$ K. (c) Electrons below and above the Fermi level flow towards a high voltage terminal under an effective electric field. (d) Electrons below and above the Fermi level flow in opposite directions under a temperature gradient.

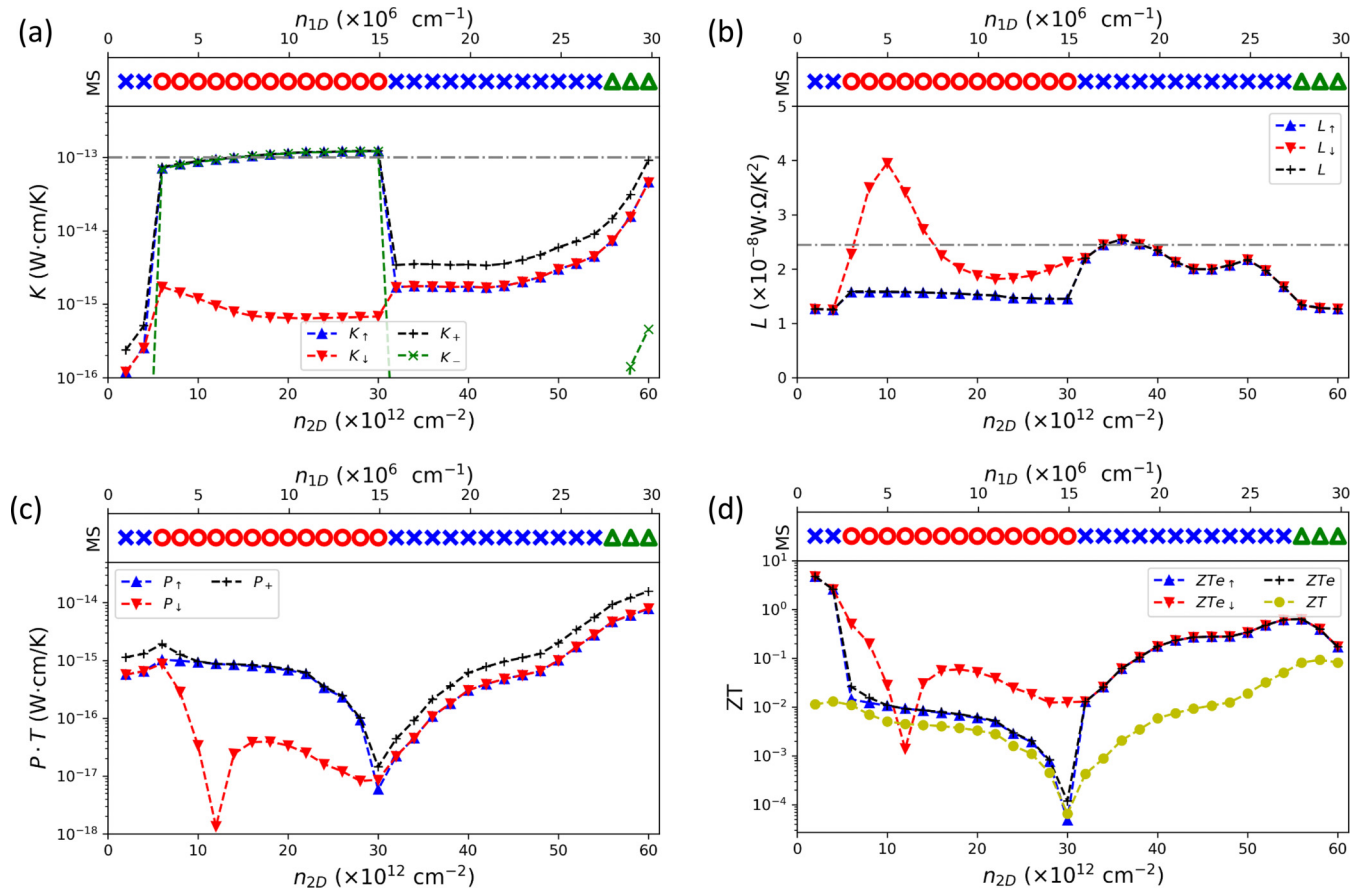

FIG. 4. (a) Thermal conductivities resulting from charge transport in a 5-nm-wide zigzag GNR at 300 K vs carrier density. The horizontal dashed line indicates lattice thermal conductivity. (b) Lorenz number, which is $K/(\sigma \cdot T)$. The horizontal dashed line indicates L_0 as defined by Eq. (20). (c) The second term in Eq. (11), which is the thermoelectric power factor P_α multiplied by temperature vs carrier density ($P_+ = P_\uparrow + P_\downarrow$). (d) Electronic thermoelectric figure of merit for spin-up ($ZTe_\uparrow$) and spin-down ($ZTe_\downarrow$) channels, the sum of them (ZTe), and the total figure of merit including lattice thermal conductivity (ZT).

We also introduce the electronic figure of merit [45], by only considering the electronic thermal conductivity:

$$ZTe_\alpha = \frac{S_\alpha^2 \sigma_\alpha T}{K_\alpha}, \tag{23}$$

which allows the separation of the two spin channels. At low carrier density in the AF states, the electronic figure of merit is large (about 5); however, the lattice thermal conductivity is two orders of magnitude higher than electronic thermal conductivity, which results in a small total figure of merit. In the other magnetic states, the electronic figure of merit is too low for energy harvesting applications, which typically require a figure of merit greater than unity.

D. Proposed experiments

The generation of a temperature gradient and the detection of a Seebeck voltage are two essential factors in measuring the spin Seebeck effect. A conventional heat reservoir ensures the local equilibrium and provides a boundary condition that electron temperatures are fixed at the phonon temperature at the contact, namely, $T_\uparrow = T_\downarrow = T_{\rm ph}$. Hence, the spin temperature is zero, $T_s = 0$. Under this condition, minority and majority spin carriers are under the same temperature gradient, and their spin voltages can be measured directly using spin-selective electrodes, such as electrodes made of magnetic metal. The schematic of the experimental setup is shown in Fig. 5(a). In the F state, one could measure $V_{\uparrow,\uparrow}$ and $V_{\downarrow,\downarrow}$ by changing the magnetization of the two electrodes to obtain the spin Seebeck voltages. In practice, the width of two spin-selective electrodes has to be designed with a coercive field different than the GNR, which allows the selection of minority or majority carriers.

Another interesting approach could be to use local probes like a scanning tunneling microscope (STM) tips. A four-probe STM has been successfully employed to measure the mean free path of carriers within GNRs [16]. The same technique but with spin polarized tips has been used to determine the chemical spin potential on the surface of topological insulators [46]. It could therefore allow a measurement of the spin Seebeck effect within a GNR with a temperature gradient, in addition to measuring the mean free path of the carriers as a function of their spin.

The spin Seebeck effect in zigzag GNRs can be used to detect spin temperature. To demonstrate this, a zigzag GNR can be part of the heat source by passing an electric current [47]. By injecting a spin-polarized electric current, the spin temperature will increase, as shown in Fig. 5(b). Similarly

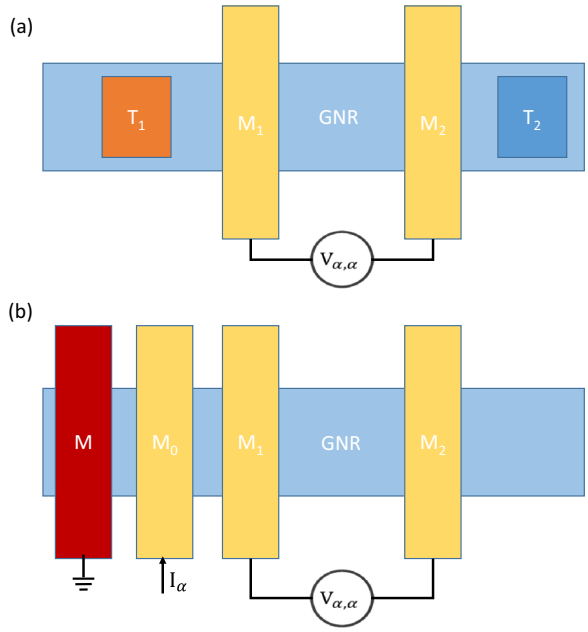

FIG. 5. (a) Proposed experimental setup to measure the spin Seebeck coefficients, using conventional thermal contacts at temperatures T_1 and T_2 and spin-selective electrodes M_1 and M_2, such as a magnetic metal, to measure spin Seebeck voltage. (b) Proposed experimental setup to demonstrate the measurement of spin temperature using spin Seebeck effect in zigzag GNR. Spin-polarized electric current is injected and serves as a heat source. Due to the weak majority carrier-lattice coupling, the spin temperature could rise.

to the previous setup, the spin Seebeck voltages could be measured using spin-selective electrodes. The Seebeck effect is expected to be very small if the spin Seebeck voltage is measured for a type of spin carrier different from that in the injected electric current. This is because no temperature gradient is supposed to be generated for the electron of that spin type. In a real situation, the temperature could nonetheless rise slightly due to the weak residual coupling with the lattice. By using the spin Seebeck effect extracted from the previous setup, one might evaluate the temperature difference for minority and majority carrier between two electrodes $\Delta T_\uparrow$ and $\Delta T_\downarrow$, and their difference would give the spin temperature ($T_s = \Delta T_\uparrow - \Delta T_\downarrow$). The minority carrier has stronger coupling to the lattice than the majority carrier, therefore $T_\downarrow \approx T_{\rm ph}$ and $T_\uparrow$ can deviate from $T_{\rm ph}$.

IV. CONCLUSION

In summary, we have demonstrated that the Seebeck coefficient of a zigzag GNR strongly depends on its magnetic states. In the F state, the Seebeck coefficient could have an opposite sign for electrons with opposite spin, which triggers the spatial separation of spin-up and spin-down electrons under a temperature gradient. Also, the spin-down channel could have a larger Seebeck coefficient than the spin-up channel. Together with weak coupling to the lattice for spin-up carriers, zigzag GNRs might serve as a spin-temperature source. These findings suggest zigzag GNRs as interesting materials for spin caloritronic applications.

ACKNOWLEDGMENTS

The authors thank Evelyne Martin for the discussion of lattice thermal conductivity. Part of the calculations used an allocation of computational resources from GENCI-IDRIS (Grant No. 2023-A0130912036).

[1] M. Slota, A. Keerthi, W. K. Myers, E. Tretyakov, M. Baumgarten, A. Ardavan, H. Sadeghi, C. J. Lambert, A. Narita, K. Müllen, and L. Bogani, Magnetic edge states and coherent manipulation of graphene nanoribbons, Nature (London) **557**, 691 (2018).

[2] V. Saraswat, R. M. Jacobberger, and M. S. Arnold, Materials science challenges to graphene nanoribbon electronics, ACS Nano **15**, 3674 (2021).

[3] W. Niu, S. Sopp, A. Lodi, A. Gee, F. Kong, T. Pei, P. Gehring, J. Nägele, C. S. Lau, J. Ma, J. Liu, A. Narita, J. Mol, M. Burghard, K. Müllen, Y. Mai, X. Feng, and L. Bogani, Exceptionally clean single-electron transistors from solutions of molecular graphene nanoribbons, Nat. Mater. **22**, 180 (2023).

[4] L. Tapaszt, G. Dobrik, P. Lambin, and L. P. Biró, Tailoring the atomic structure of graphene nanoribbons by scanning tunnelling microscope lithography, Nat. Nanotechnol. **3**, 397 (2008).

[5] D. V. Kosynkin, A. L. Higginbotham, A. Sinitskii, J. R. Lomeda, A. Dimiev, B. K. Price, and J. M. Tour, Longitudinal unzipping of carbon nanotubes to form graphene nanoribbons, Nature (London) **458**, 872 (2009).

[6] I. Palacio, A. Celis, M. N. Nair, A. Gloter, A. Zobelli, M. Sicot, D. Malterre, M. S. Nevius, W. A. de Heer, C. Berger, E. H. Conrad, A. Taleb-Ibrahimi, and A. Tejeda, Atomic structure of epitaxial graphene sidewall nanoribbons: Flat graphene, miniribbons, and the confinement gap, Nano Lett. **15**, 182 (2015).

[7] P. Ruffieux, S. Wang, B. Yang, C. Sanchez, J. Liu, T. Dienel, L. Talirz, P. Shinde, C. A. Pignedoli, D. Passerone, T. Dumslaff, X. Feng, K. Muellen, and R. Fasel, On-surface synthesis of graphene nanoribbons with zigzag edge topology, Nature (London) **531**, 489 (2016).

[8] L. Chen, L. He, H. S. Wang, H. Wang, S. Tang, C. Cong, H. Xie, L. Li, H. Xia, T. Li, T. Wu, D. Zhang, L. Deng, T. Yu, X. Xie, and M. Jiang, Oriented graphene nanoribbons embedded in hexagonal boron nitride trenches, Nat. Commun. **8**, 14703 (2017).

[9] L. Yang, C.-H. Park, Y.-W. Son, M. L. Cohen, and S. G. Louie, Quasiparticle Energies and Band Gaps in Graphene Nanoribbons, Phys. Rev. Lett. **99**, 186801 (2007).

[10] K. Nakada, M. Fujita, G. Dresselhaus, and M. S. Dresselhaus, Edge state in graphene ribbons: Nanometer size effect and edge shape dependence, Phys. Rev. B **54**, 17954 (1996).

[11] K. Wakabayashi, K.-i. Sasaki, T. Nakanishi, and T. Enoki, Electronic states of graphene nanoribbons and analytical solutions, Science and Technology of Advanced Materials **11**, 054504 (2010).

[12] M. Fujita, K. Wakabayashi, K. Nakada, and K. Kusakabe, Peculiar localized state at zigzag graphite edge, J. Phys. Soc. Jpn. **65**, 1920 (1996).

[13] J. Jung and A. H. MacDonald, Carrier density and magnetism in graphene zigzag nanoribbons, Phys. Rev. B **79**, 235433 (2009).

[14] J. Li, Y.-M. Niquet, and C. Delerue, Magnetic-Phase Dependence of the Spin Carrier Mean Free Path in Graphene Nanoribbons, Phys. Rev. Lett. **116**, 236602 (2016).

[15] G. Z. Magda, X. Jin, I. Hagymasi, P. Vancso, Z. Osvath, P. Nemes-Incze, C. Hwang, L. P. Biro, and L. Tapaszto, Room-temperature magnetic order on zigzag edges of narrow graphene nanoribbons, Nature (London) **514**, 608 (2014).

[16] J. Baringhaus, M. Ruan, F. Edler, A. Tejeda, M. Sicot, Taleb-IbrahimiAmina, A.-P. Li, Z. Jiang, E. H. Conrad, C. Berger, C. Tegenkamp, and W. A. de Heer, Exceptional ballistic transport in epitaxial graphene nanoribbons, Nature (London) **506**, 349 (2014).

[17] V. S. Prudkovskiy, Y. Hu, K. Zhang, Y. Hu, P. Ji, G. Nunn, J. Zhao, C. Shi, A. Tejeda, D. Wander, A. De Cecco, C. B. Winkelmann, Y. Jiang, T. Zhao, K. Wakabayashi, Z. Jiang, L. Ma, C. Berger, and W. A. de Heer, An epitaxial graphene platform for zero-energy edge state nanoelectronics, Nat. Commun. **13**, 7814 (2022)

[18] R. E. Blackwell, F. Zhao, E. Brooks, J. Zhu, I. Piskun, S. Wang, A. Delgado, Y.-L. Lee, S. G. Louie, and F. R. Fischer, Spin splitting of dopant edge state in magnetic zigzag graphene nanoribbons, Nature (London) **600**, 647 (2021).

[19] G. E. W. Bauer, E. Saitoh, and B. J. van Wees, Spin caloritronics, Nat. Mater. **11**, 391 (2012).

[20] K. Uchida, S. Takahashi, K. Harii, J. Ieda, W. Koshibae, K. Ando, S. Maekawa, and E. Saitoh, Observation of the spin Seebeck effect, Nature (London) **455**, 778 (2008).

[21] K. Uchida, J. Xiao, H. Adachi, J. Ohe, S. Takahashi, J. Ieda, T. Ota, Y. Kajiwara, H. Umezawa, H. Kawai, G. E. W. Bauer, S. Maekawa, and E. Saitoh, Spin Seebeck insulator, Nat. Mater. **9**, 894 (2010).

[22] C. M. Jaworski, J. Yang, S. Mack, D. D. Awschalom, J. P. Heremans, and R. C. Myers, Observation of the spin-Seebeck effect in a ferromagnetic semiconductor, Nat. Mater. **9**, 898 (2010).

[23] E.-J. Guo, J. Cramer, A. Kehlberger, C. A. Ferguson, D. A. MacLaren, G. Jakob, and M. Kläui, Influence of Thickness and Interface on the Low-Temperature Enhancement of the Spin Seebeck Effect in YIG Films, Phys. Rev. X **6**, 031012 (2016).

[24] L. Gravier, S. Serrano-Guisan, F. Reuse, and J.-P. Ansermet, Spin-dependent Peltier effect of perpendicular currents in multilayered nanowires, Phys. Rev. B **73**, 052410 (2006).

[25] J. Flipse, F. L. Bakker, A. Slachter, F. K. Dejene, and B. J. van Wees, Direct observation of the spin-dependent Peltier effect, Nat. Nanotechnol. **7**, 166 (2012).

[26] M. Zeng, W. Huang, and G. Liang, Spin-dependent thermoelectric effects in graphene-based spin valves, Nanoscale **5**, 200 (2013).

[27] X. Chen, Y. Liu, B. L. Gu, W. Duan, and F. Liu, Giant room-temperature spin caloritronics in spin-semiconducting graphene nanoribbons, Phys. Rev. B **90**, 121403(R) (2014).

[28] M.-X. Zhai and X.-F. Wang, Atomistic switch of giant magnetoresistance and spin thermopower in graphene-like nanoribbons, Sci. Rep. **6**, 36762 (2016).

[29] F. Ildarabadi and R. Farghadan, Spin-thermoelectric transport in nonuniform strained zigzag graphene nanoribbons, Phys. Rev. B **103**, 115424 (2021).

[30] Y. Ni, G. Deng, J. Li, H. Hua, and N. Liu, The strain-tuned spin Seebeck effect, spin polarization, and giant magnetoresistance of a graphene nanobubble in zigzag graphene nanoribbons, ACS Omega **6**, 15308 (2021).

[31] N. F. Mott, The electrical conductivity of transition metals, Proc. R. Soc. A **153**, 699 (1936).

[32] A. Fert and I. A. Campbell, Two-Current Conduction in Nickel, Phys. Rev. Lett. **21**, 1190 (1968).

[33] L. Yi, D. Yang, M. Liu, H. Fu, L. Ding, Y. Xu, B. Zhang, L. Pan, and J. Q. Xiao, Concepts of spin Seebeck effect in ferromagnetic metals, Adv. Funct. Mater. **30**, 2004024 (2020).

[34] M. Gurram, S. Omar, and B. J. van Wees, Electrical spin injection, transport, and detection in graphene-hexagonal boron nitride van der Waals heterostructures: Progress and perspectives, 2D Mater. **5**, 032004 (2018).

[35] V. H. Guarochico-Moreira, J. L. Sambricio, K. Omari, C. R. Anderson, D. A. Bandurin, J. C. Toscano-Figueroa, N. Natera-Cordero, K. Watanabe, T. Taniguchi, I. V. Grigorieva, and I. J. Vera-Marun, Tunable spin injection in high-quality graphene with one-dimensional contacts, Nano Lett. **22**, 935 (2022).

[36] N. Ashcroft and N. Mermin, *Solid State Physics* (Saunders College Publishing, USA, 1976), Chap. 13, p. 252.

[37] J. Li, H. P. C. Miranda, Y.-M. Niquet, L. Genovese, I. Duchemin, L. Wirtz, and C. Delerue, Phonon-limited carrier mobility and resistivity from carbon nanotubes to graphene, Phys. Rev. B **92**, 075414 (2015).

[38] W. Zhang, C. Delerue, Y.-M. Niquet, G. Allan, and E. Wang, Atomistic modeling of electron-phonon coupling and transport properties in *n*-type [110] silicon nanowires, Phys. Rev. B **82**, 115319 (2010).

[39] D. G. Miller, Thermodynamics of irreversible processes. the experimental verification of the onsager reciprocal relations, Chem. Rev. **60**, 15 (1960).

[40] Y. M. Zuev, W. Chang, and P. Kim, Thermoelectric and Magnetothermoelectric Transport Measurements of Graphene, Phys. Rev. Lett. **102**, 096807 (2009).

[41] R. Franz and G. Wiedemann, Ueber die wärmeleitungsfähigkeit der metalle, Ann. Phys. (Leipzig) **165**, 497 (1853).

[42] A. Garg, D. Rasch, E. Shimshoni, and A. Rosch, Large Violation of the Wiedemann-Franz Law in Luttinger Liquids, Phys. Rev. Lett. **103**, 096402 (2009).

[43] Y. Wang, B. Qiu, and X. Ruan, Edge effect on thermal transport in graphene nanoribbons: A phonon localization mechanism beyond edge roughness scattering, Appl. Phys. Lett. **101**, 013101 (2012).

[44] J. Hu, X. Ruan, and Y. P. Chen, Thermal conductivity and thermal rectification in graphene nanoribbons: A molecular dynamics study, Nano Lett. **9**, 2730 (2009).

[45] J. Li, T. C. A. Yeung, and C. H. Kam, The upper limit of thermoelectric figure of merit: Importance of electronic thermoelectric efficiency, J. Phys. D **45**, 085102 (2012).

[46] S. M. Hus, X.-G. Zhang, G. D. Nguyen, W. Ko, A. P. Baddorf, Y. P. Chen, and A.-P. Li, Detection of the Spin-Chemical Potential in Topological Insulators using Spin-Polarized Four-Probe STM, Phys. Rev. Lett. **119**, 137202 (2017).

[47] J. F. Sierra, I. Neumann, J. Cuppens, B. Raes, M. V. Costache, and S. O. Valenzuela, Thermoelectric spin voltage in graphene, Nat. Nanotechnol. **13**, 107 (2018).